Research Article

Activating the Stepwise Intercalation−Conversion Reaction of Layered Copper Sulfide toward Extremely High Capacity Zinc-Metal-Free Anodes for Rocking-Chair Zinc-Ion Batteries

Zeheng Lv, Bo Wang, Minghui Ye, Yufei Zhang, Yang Yang,* and Cheng Chao Li*

Cite This: https://doi.org/10.1021/acsami.1c21168

Read Online

ACCESS | Metrics & More | Article Recommendations | Supporting Information

ABSTRACT: Conventional zinc-ion batteries (ZIBs) are severely hindered by the inherent drawbacks of Zn metal anodes including dendrite growth, side reactions, and interface passivation. Developing intercalation-type anodes to fabricate rocking-chair ZIBs is a promising approach to overcome the above issues. However, the low capacity resulting from the limited transfer electron number of intercalation reactions impedes their practical applications. Herein, we report an effective strategy to break the capacity limit of layered CuS materials as a Zn-metal-free anode through activating its intrinsic conversion reaction. It is found that the preintercalation of cetyltrimethylammonium bromide in CuS (CuS@CTMAB) significantly lowers the energy barrier of the conversion reaction, thus realizing a record-breaking capacity (367.4 mAh g^{-1} at 0.1 A g^{-1}) as a Zn-metal-free anode based on the reversible conversion of Cu^{2+}/Cu^{0}. Theoretical calculation, ex situ microscopy, and spectroscopy results verify that the characteristic stepwise intercalation−conversion reaction route occurred in CuS@CTMAB. Moreover, the moderate structure transformation and good electronic conduction during the phase evolution process led to excellent cycling stability and high rate performance. Consequently, the rocking-chair ZIB full battery system utilizing CuS@CTMAB and Zn^{2+}-preintercalated MnO_2 as the anode and cathode, respectively, exhibits exceptional capacity retention of 93.9% up to 8000 cycles at 2 A g^{-1}. Besides, the CuS@CTMAB anode is also compatible with high-voltage Prussian blue cathodes, demonstrating its outstanding practicality.

KEYWORDS: copper sulfide, anode material, record-breaking capacity, rocking-chair-type aqueous zinc-ion batteries, intercalation−conversion reactions
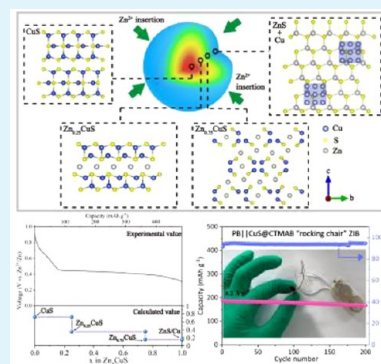
1. INTRODUCTION

Reliable electrochemical energy storage (EES) technology is essential for sustainable societal development and reduction of our reliance on fossil fuels. The EES field has been dominated by lithium-ion batteries (LIBs) since their first commercialization by Sony Corporation in 1991.[1] However, the inherent drawbacks of limited lithium resources, high cost, and potential security issues critically impede their applications in large-scale EES devices.[2,3] Particularly, the high-profile spontaneous combustion and explosion incidents of LIBs used in electrical vehicles and aircraft have raised intense concerns about their reliability. Most catastrophic accidents of LIBs are triggered by self-propagating exothermic reactions between electrolyte materials and flammable organic electrolytes.[4] Therefore, developing novel metal-ion batteries with aqueous electrolytes to enhance intrinsic safety and dependability has attracted extensive attention.[5−7] Among them, aqueous zinc-ion batteries (ZIBs) are regarded as one of the most fascinating alternative technologies for large-scale applications, owing to the characteristics of low cost, environmental friendliness, and superior ionic conductivity.[8,9]

The classical configuration of aqueous ZIBs is based on intercalation-type cathodes and the Zn metal anode in mild acid electrolytes.[10] The reversible insertion and extraction of Zn^{2+} in cathode materials such as MnO_2,[11,12] vanadium oxides,[13] vanadium-based NASICONs,[14,15] Prussian blue analogues,[16] and organic compounds[17] produce relatively high potentials and capacities. On the anode side, Zn metal is the most commonly used anode material, which possesses high theoretical capacity (820 mAh g^{-1}) and low electrochemical potential (−0.763 V vs SHE).[18] Despite the above merits, the unsatisfactory deposition/stripping Coulombic efficiency (CE), low utilization of the Zn metal anode resulting from dendrite growth, self-corrosion, and passivation issues severely deteriorate the lifespan and energy density of

ZIBs.[19,20] Although many strategies including electrode structural design,[21,22] surface modification,[23−26] and Zn alloying[27,28] have been proposed to improve the electrochemical performance of Zn metal anodes, resolving these problems thoroughly is still difficult. It should be noticed that the Zn dendrites issue may be exponentially aggravated at high loading mass and high current densities, which will ruin the battery under practical conditions.[29,30]

Review of the development history of LIBs shows that the Li dendrites issue also perplexed people for years[31] until, in the 1980s, a carbon-based material was adopted by Akira Yoshino to replace Li metal as the anode. This significant breakthrough was jointly awarded the 2019 Nobel Prize in chemistry.[32] This Li-metal-free prototype system is called a "rocking-chair" battery, in which ions are transferred from one side to the other with two different intercalation compounds as a cathode and anode. Inspired by this, designing "rocking-chair" ZIBs seems to open a new venue for overcoming the inherent drawbacks rooted in the Zn metal anode, and the greatest challenge lies in exploiting suitable intercalation anode materials.[33,34] The chevrel phase Mo_6S_8 was first proposed as an intercalation anode material due to its unique tridirectional channels, which are suitable for hosting Zn^{2+}.[35] But the low capacity ($\sim$60 mAh g^{-1} at 0.18 A g^{-1}) restricts its wide application. Recently, Li et al. reported a pioneering work using layer structured $Na_{0.14}TiS_2$ for accommodating Zn^{2+}, achieving a relatively higher reversible capacity of 140 mAh g^{-1} at 0.05 A g^{-1}.[36] However, the additional time-consuming electrochemical pre-sodiation method impedes a broader application of this approach. Our group also demonstrated $Cu_{2−x}Se$ as a novel intercalation anode, which exhibits a considerable capacity of 152.1 mAh g^{-1} at 0.2 A g^{-1}.[37] Despite the great advancement, the Zn^{2+} storage capacity of intercalation anode materials is far from the requirements needed for practical applications, which has become the bottleneck for developing high-performance rocking-chair ZIBs.

The theoretical capacity of intercalation compounds is determined by the transfer electron number of transition metal redox couples in the host crystal lattice.[38] And the intercalation process of ions is always accompanied by the reduced valence state of the host metal ion, for instance, Ti^{4+} to Ti^{3+} in TiS_2. To break the constraint of the (de)intercalation reaction, conversion reaction mechanism anode materials such as metal oxides and metal sulfides have been investigated in LIBs to give rise to large capacities.[39,40] However, most previously reported anode materials in rocking-chair ZIBs are still based on the simple intercalation reaction mechanism. Interestingly, the Cu^+-based materials such as CuI, Cu_2S, and Cu_2O are demonstrated to work with the conversion reaction in aqueous Zn-ion batteries.[41,42] Moreover, with the conversion mechanism, Cu^+-based materials deliver high capacity, which can largely improve the energy density of ZIBs. Herein, we propose CTMAB (hexadecyltrimethylammonium bromide)-preintercalated CuS (CuS@CTMAB) with enlarged interlayer spacings as a high-capacity anode material for rocking-chair ZIBs. Theoretical calculation, ex situ microscopy, and spectroscopy results reveal that Zn^{2+} storage in CuS@CTMAB is based on the unique intercalation−conversion reaction mechanism, contributing to high Zn^{2+} storage capacity, fast electrochemical kinetics, and good structural stability during cycling. As a result, the CuS@CTMAB anode with the suitable working potential of $\sim$0.37 V (vs Zn^{2+}/Zn) displays an impressive reversible capacity (350.3

mAh g^{-1} at 0.2 A g^{-1}) and outstanding cycling stability (0.012% capacity decay per cycle over 3000 cycles). Moreover, the CuS@CTMAB anode is coupled with MnO_2 and $CoFe(CN)_6$ Prussian blue cathodes to fabricate rocking-chair zinc-ion full batteries to comprehensively verify its feasibility in practical applications.

2. EXPERIMENTAL SECTION

2.1. Synthesis of CuS@CTMAB. CuS@CTMAB was prepared by a previously reported hydrothermal method with minor modification.[43] First, a mixture solution containing 10 mL of ethylene glycol and 30 mL of deionized water was prepared. Then, 0.483 g of copper(II) nitrate hydrate ($Cu(NO_3)_3\cdot3H_2O$, Aladdin), 0.380 g of thiourea (CH_4N_2S, Aladdin), and 0.2 g of CTMAB (Aladdin) were dissolved in the above solution with magnetic stirring for about 10 min to form a homogeneous solution. The solution was transferred into a 50 mL Teflon-lined autoclave and treated at 100 °C for 18 h. Finally, the as-prepared products were washed with deionized water and ethanol and dried at 60 °C for 24 h.

2.2. Synthesis of Pristine CuS. Amounts of 0.483 g of copper(II) nitrate hydrate ($Cu(NO_3)_3\cdot3H_2O$, Aladdin) and 0.380 g of thiourea (CH_4N_2S, Aladdin) were dissolved in the solution containing 10 mL of ethylene glycol and 30 mL of deionized water with magnetic stirring to form a homogeneous solution. Then, the mixture was processed the same as CuS@CTMAB.

2.3. Synthesis of $CoFe(CN)_6$. $CoFe(CN)_6$ was prepared by a previously reported aqueous reaction method with minor modification.[44] First, a mixture solution A containing 0.0747 g of $Co(CH_3COO)_2\cdot4H_2O$ (Aladdin) and 300 mL of deionized water was prepared. Then, 0.494 g of $K_3[Fe(CN)_6]$ (Aladdin) and 10.5 g of sodium dodecyl sulfate (SDS, Aladdin) were dissolved in 300 mL of deionized water to obtain solution B. Solution A was transferred into solution B to form solution C. After aging at room temperature for 48 h, the resulting precipitate was washed via deionized water. Finally, $KCoFe(CN)_6$ was obtained after freeze-drying for 48 h.

The $CoFe(CN)_6$ was in situ transformed through the electrochemical extraction of K^+ from $KCoFe(CN)_6$ in 4 M $Zn(OTf)_2$ electrolyte in a Zn‖KCoFe $(CN)_6$ half-cell by charging at 0.1 A g^{-1} with the upper cutoff capacity of 140 mAh g^{-1}.

2.4. Sample Characterization. X-ray diffraction (XRD) measurements of the synthesized samples were carried out using a Rigaku MiniFlex600 powder X-ray diffractometer (Cu Kα radiation, λ = 0.15418 nm). Raman spectra were collected through a Raman spectrometer (LabRAM HR, Horiba JobinYvon). X-ray photoelectron spectroscopy (XPS) spectra were obtained by an ESCALAB 250Xi spectrometer (ThermoFischer Scientific). Scanning electron microscopy (SEM) images and transmission electron microscopy (TEM) images were characterized by a scanning electron microscope (SU-8010, Hitachi) and transmission electron microscope (JEM-2100, FEI), respectively.

2.5. Electrochemical Measurements. *2.5.1. Fabrication of the Working Electrodes.* Amounts of 70 wt % active material (CuS@CTMAB or CuS samples), 20 wt % carbon black, and 10 wt % binder [poly(vinylidene fluoride), PVDF] were dispersed evenly in N-methyl-2-pyrrolidone (NMP) to form a slurry. The slurry was coated onto Cu foil, and then dried in a vacuum oven overnight at 80 °C. The loading mass of active materials on the Cu foil was about 1 mg cm^{-2}.

2.5.2. Assembling the CR-2032-Type Half-Cells. With Zn foil as the counter electrode, a glass fiber filter (GF/D, Whatman) as the separator, and 2 M $ZnSO_4$ aqueous solution as the electrolyte, the half-cells can be assembled.

Galvanostatic charge−discharge tests were executed via a Neware battery testing system. Cyclic voltammetry (CV) curves and electrochemical impedance spectra (EIS) were obtained by an electrochemical workstation (Interface 1010B, Gamry Instruments).

2.5.3. Assembling the CR-2032-Type Full Cells. The CuS@CTMAB anode electrode was coupled with a MnO_2 and $CoFe(CN)_6$
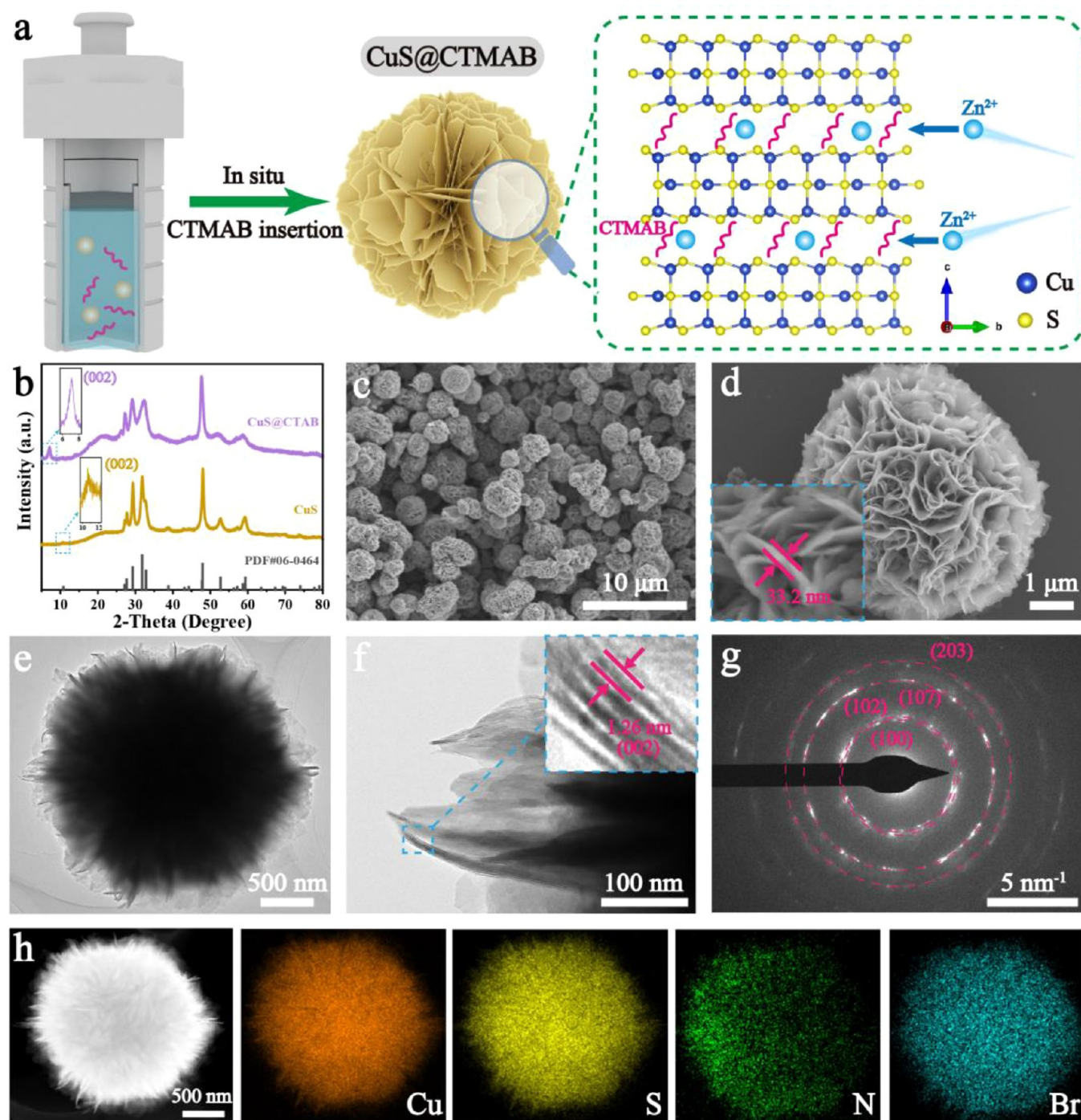
Figure 1. (a) Schematic illustration of the synthetic procedure for CuS@CTMAB and its Zn^{2+} intercalation process. (b) XRD patterns of CuS and CuS@CTMAB samples. (c and d) SEM images of CuS@CTMAB. (e) The TEM image and (f) HR-TEM image of a single CuS@CTMAB particle. (g) SAED patterns of CuS@CTMAB. (h) The HAADF image and corresponding elemental mapping of a single CuS@CTMAB particle.

cathode with 2 M $ZnSO_4$ + 0.1 M $MnSO_4$ and 4 M $Zn(OTf)_2$ aqueous solutions as the electrolyte, respectively.

The MnO_2 cathode was prepared by using commercial MnO_2 (Aladdin, 98%) as the active material, and the loading mass of MnO_2 was ∼2 mg cm^{-2}. Then, the MnO_2 cathode was assembled into half-cells with Zn foil, which were discharged with a 32 h constant-voltage (0.8 V) step at 0.1 A g^{-1} to form the Zn-insertion MnO_2 electrodes (denoted as Zn_xMnO_2). Consequently, the Zn_xMnO_2 electrodes were obtained to fabricate the CuS@CTMAB ‖ Zn_xMnO_2 full cells with 2 M $ZnSO_4$ + 0.1 M $MnSO_4$ aqueous electrolyte. The N/P (negative capacity/positive capacity) ratio of CuS@CTMAB ‖ Zn_xMnO_2 is about 0.88.

The $CoFe(CN)_6$ cathode was prepared via an electrochemical method, and the loading mass of CoFe $(CN)_6$ was ∼8 mg cm^{-2}. After electrochemically extracting K$^+$ from $KCoFe(CN)_6$, the Zn‖KCoFe $(CN)_6$ half-cell was discharged/charged with 10 cycles, and the Zn^{2+}-preintercalated $CoFe(CN)_6$ electrodes (denoted as $Zn_xCoFe(CN)_6$) were obtained at the end of the last discharge step. Finally, the CuS@CTMAB ‖$Zn_xCoFe(CN)_6$ full cells with 4 M $Zn(OTf)_2$ aqueous electrolyte were fabricated. The N/P ratio of CuS@CTMAB ‖ $Zn_xCoFe(CN)_6$ is about 0.67.

2.6. DFT Calculations. All first-principles calculations were performed within the Vienna Ab initio Simulation Package (VASP) based on density functional theory (DFT).[45] The projector
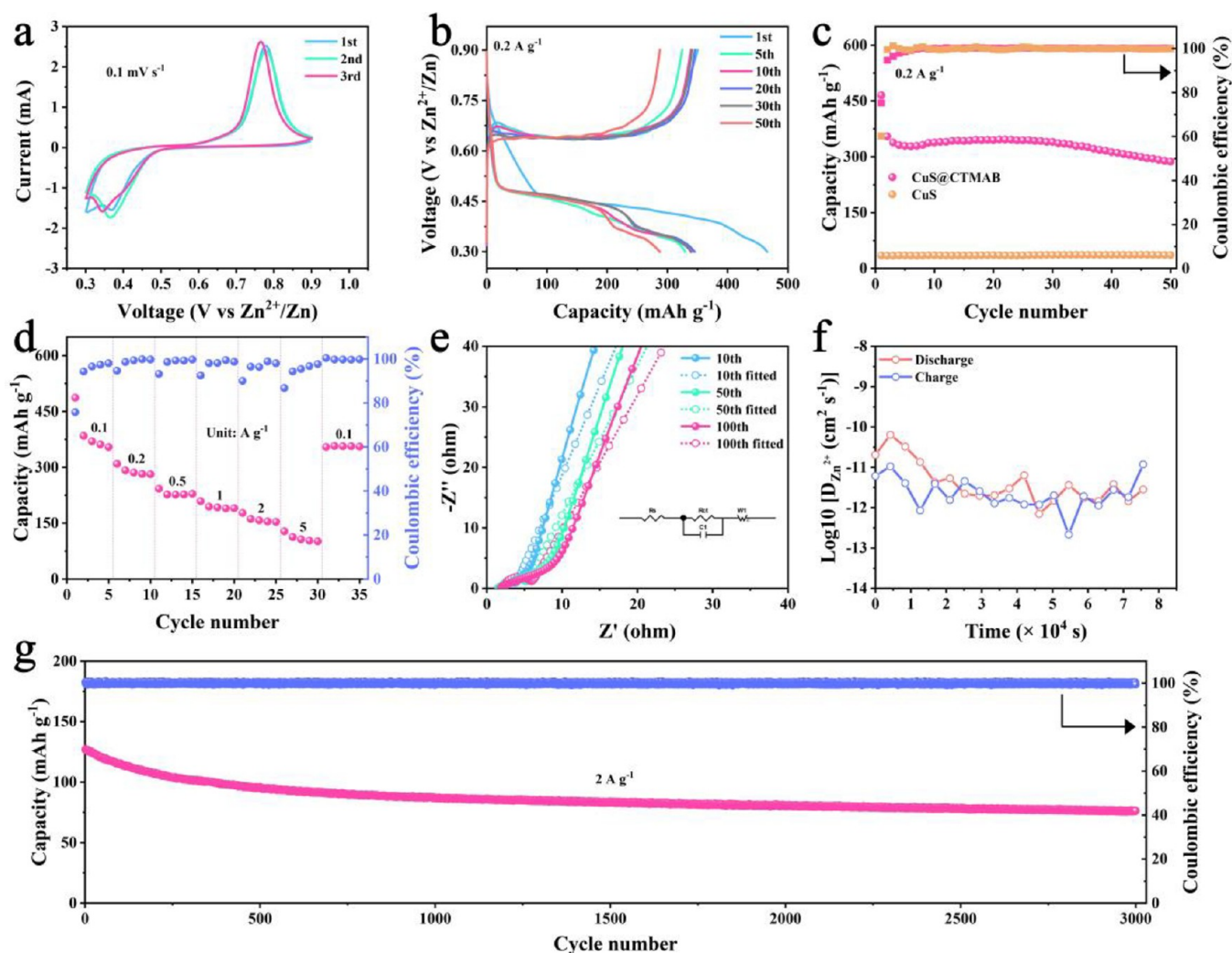
Figure 2. (a) Cyclic voltammograms of the CuS@CTMAB electrode at a scan rate of 0.1 mV s^{-1} between 0.3 and 0.9 V (vs Zn^{2+}/Zn). (b) Typical charge−discharge profiles of the CuS@CTMAB at 0.2 A g^{-1}. (c) Cycling performance of the CuS and CuS@CTMAB at 0.2 A g^{-1}. (d) Rate performance of the CuS@CTMAB electrode. (e) EIS of the CuS@CTMAB electrode after different cycles. (f) The calculated Zn^{2+} diffusion coefficients of the CuS@CTMAB electrode from GITT. (g) Long-term cycling performance of the CuS@CTMAB at the high current density of 2 A g^{-1}.

augmented wave (PAW) potentials were used to deal with the electronic exchange-correlation interaction along with the GGA functional in the parametrization of the Perdew, Burke, and Ernzerhof (PBE) pseudopotential.[46] A plane wave representation for the wave function with a cutoff energy of 450 eV was applied. Geometry optimizations were performed using a conjugate gradient minimization until all the forces acting on the ions were less than 0.02 eV/Å per atom. A 15 Å vacuum in the z direction was used to separate the slabs. In the calculations, a k-point mesh with a spacing of ca. 0.03 Å^{-1} was adopted.

3. RESULTS AND DISCUSSION

3.1. Material Structure and Composition Characterization. CuS@CTMAB was prepared through a facile one-step hydrothermal reaction method; meanwhile, the in situ chemical preintercalation of CTMAB in the interlayer spaces of CuS is expected to further enlarge the interlayer spacings (Figure 1a).[43] From the XRD patterns of the CuS and CuS@CTMAB samples (Figure 1b), all Bragg diffraction peaks can be exactly indexed to the hexagonal CuS phase (JCPDS no. 06-0464) without any impurities. It should be noticed that the (002) peak of CuS@CTMAB shifts toward a lower degree

(6.92°) compared with that of pristine CuS (10.81°), demonstrating that the interlayer spacing of CuS is successfully enlarged after the intercalation of CTMAB. Accordingly, the d-spacing of (002) is calculated to be 1.26 nm based on the Bragg equation ($2d \sin \theta = n\lambda$), which is much larger than the standard value of 0.82 nm. Although CuS has exhibited impressive Li$^+$ and Na$^+$ storage performance, the solid-state diffusion of Zn^{2+} in the host structure is much slower than that of Li$^+$ and Na$^+$, due to the strong electrostatic interaction. Therefore, the enlarged interlayer spacing of CuS should facilitate the intercalation of Zn^{2+}. To further investigate the microstructure of the as-prepared CuS and CuS@CTMAB samples, SEM and TEM were employed (Figure 1c−h). The CuS@CTMAB sample displays a flower-like micromorphology with a diameter ranging from 1 to 5 μm (Figure 1c), and each individual microflower is composed of nanosheets having a thickness of ∼30 nm (Figure 1d), whereas the CuS sample without added CTMAB exhibits denser microspheres with a similar particle size as that of CuS@CTMAB (Figure S1). It can be deemed that CTMAB is not only an interlayer pillar in CuS@CTMAB but also acts as a functional structure-directing
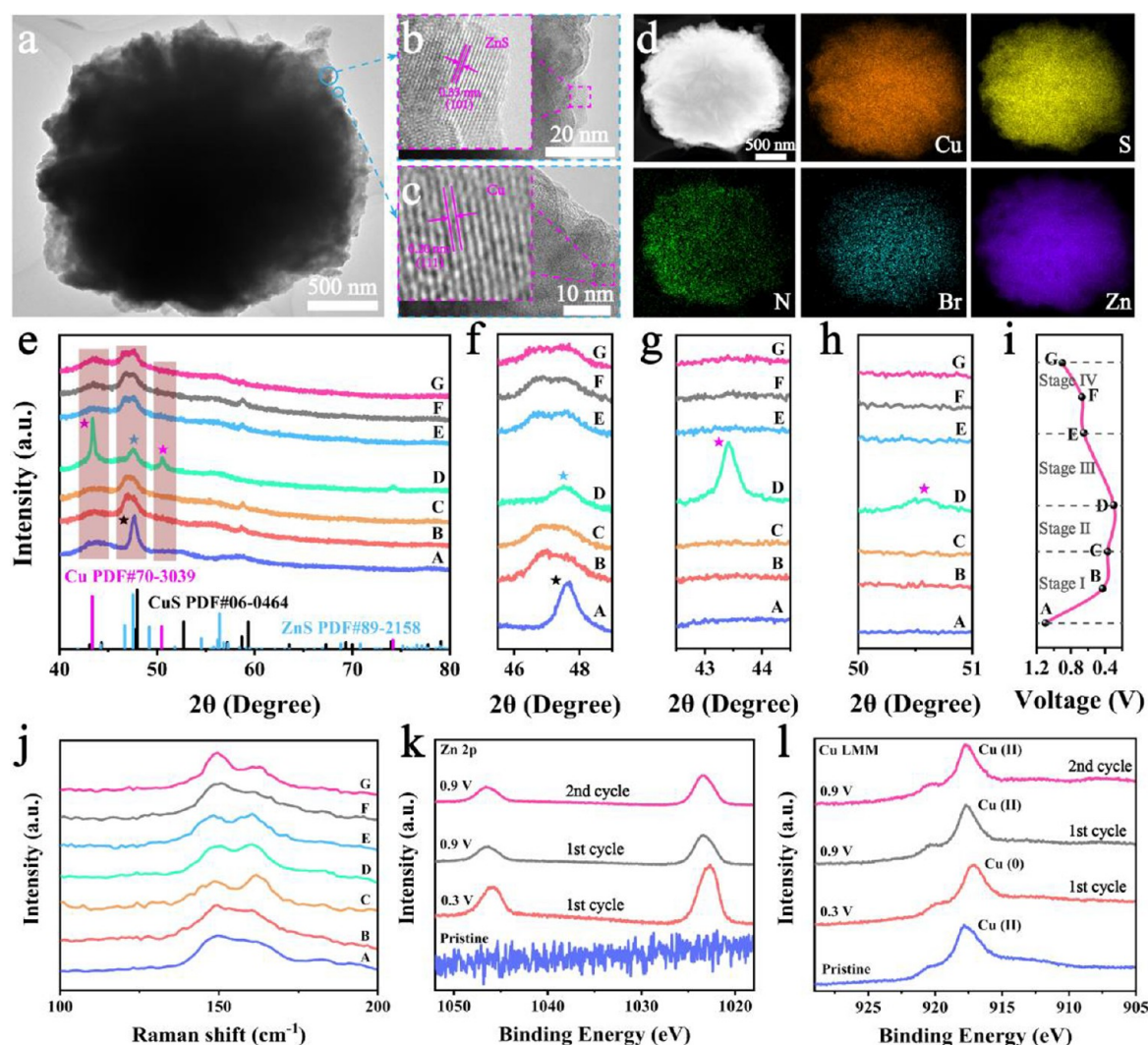
Figure 3. (a) TEM, (b and c) enlarged HR-TEM, and (d) elemental mapping images of the CuS@CTMAB electrode after being discharged to 0.3 V in the initial cycle. (e−i) Ex situ XRD patterns of the CuS@CTMAB electrodes collected at different charge/discharge states as indicated in the corresponding voltage profile. (j) Ex situ Raman spectra of the CuS@CTMAB electrodes. (k) Zn 2p XPS spectra and (l) Auger Cu LMM spectra of the CuS@CTMAB electrodes in the pristine and fully discharge/charge states.

agent to affect the morphology and surface area during the hydrothermal reaction. The TEM image (Figure 1e) further confirms that the CuS@CTMAB microflower is stacked by ultrathin nanosheets. The high-resolution transmission electron microscopy (HR-TEM) image of the CuS@CTMAB nanosheets near the edge (Figure 1f) shows clear lattice fringes with a *d*-spacing of ∼1.26 nm, matching well the calculated value of the (002) plane by XRD. The SAED (selected area electron diffraction) patterns (Figure 1g) present obvious diffraction rings, corresponding to the (100), (102), (107), and (203) planes of hexagonal phase CuS, which are indicative of both the polycrystalline nature and good crystalline degree. In the HAADF (high-angle annular dark field) and corresponding elemental mapping images (Figure 1h), Cu, S, N, O, and Br elements are uniformly distributed, suggesting that CTMAB is homogeneously intercalated into the interior crystalline structure of CuS.

3.2. Electrochemical Performance of CR-2032-Type Half-Cells.
The electrochemical Zn^{2+} storage properties of CuS and CuS@CTMAB were first evaluated in CR-2032-type coin cells with Zn metal as the anode (Figure 2), as depicted in

the CV curves of the CuS@CTMAB electrode in 2 M $ZnSO_4$ aqueous electrolyte in the voltage range of 0.3−0.9 V at a scan rate of 0.1 mV s^{-1} (Figure 2a). One peak at ∼0.37 V was detected in the cathodic process, which can be attributed to the electrochemical reduction of CuS with Zn^{2+}. Moreover, an anodic peak is clearly observed at about 0.77 V in the anodic process, which corresponds to the extraction of Zn^{2+}. In the subsequent cycles, the peak intensities are nearly overlapped, revealing the good reversibility of the Zn^{2+} insertion and extraction reactions. Then, the electrochemical performance of both samples was investigated through galvanostatic discharge−charge tests. The CuS@CTMAB electrode delivers initial discharge and charge capacities of 465.3 and 350.3 mAh g^{-1}, showing a first-cycle CE of 75.3% at 0.2 A g^{-1} (Figure 2b). The nonreversible capacity loss during the initial cycle may be assigned to the trapping of a small amount of Zn^{2+} in the host structure and side reactions such as formation of hydroxide sulfate zinc compounds. It can be seen that Zn^{2+} insertion into CuS@CTMAB mainly occurs at a voltage range between 0.45 and 0.3 V (vs Zn^{2+}/Zn), which is obviously above the Zn deposition/stripping electrochemical potential. The CuS@
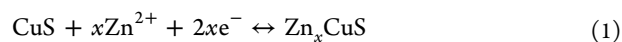
CTMAB electrode having a moderate working voltage serving as the anode can not only prevent the formation of Zn dendrites but also fundamentally eliminate the hydrogen evolution reaction (HER). Recent studies about Zn metal anodes demonstrated that the side reaction of HER will result in electrochemical corrosion and the formation of a passivation film, lowering the CE and lifespan dramatically. After 50 discharge–charge cycles at 0.2 A g^{-1}, the reversible capacity of the CuS@CTMAB electrode is maintained at 287.5 mAh g^{-1} (Figure 2c). Surprisingly, the reversible capacity of pristine CuS is only ~35.3 mAh g^{-1} at 0.2 A g^{-1}, implying that Zn^{2+} may not be smoothly inserted into CuS without the chemical preintercalation of CTMAB. Importantly, the CE of CuS@CTMAB rapidly increases to above 99.5% after only 15 cycles and is maintained steadily in the subsequent cycles, revealing the good reversibility of the material. The amount of Zn needed in the anode is far beyond the cathode capacity when using metallic Zn as the anode due to its unsatisfactory CE (~95%) in aqueous electrolytes,[47−49] which should definitely decrease the energy density of ZIBs. The ultrahigh CE of the CuS@CTMAB electrode efficiently ensures the high utilization of the electrode capacity when matching with the cathode.

The rate performance of the CuS@CTMAB electrode is depicted in Figure 2d. It could deliver an average capacity of 367.4, 290.0, 230.4, 195.1, and 160.8 mAh g^{-1} at a current density of 0.1, 0.2, 0.5, 1, and 2 A g^{-1}, respectively. Even at the extremely high current density of 5 A g^{-1}, a high reversible capacity of 101.2 mAh g^{-1} can still be retained. As the current density decreases to 0.1 A g^{-1} again, the discharge capacity of the CuS@CTMAB electrode rapidly reproduces to 357.2 mAh g^{-1}, indicating the remarkable endurance for fast charge/discharge. Furthermore, the long-term cycling stability is examined at a high current density of 2 A g^{-1} (Figure 2g and Figure S2). The CuS@CTMAB electrode can achieve a considerable capacity retention of 61.1% after 3000 cycles, and the CE remains up to 99.9% during the whole cycling test. To further understand the good rate capability and cycling stability of the CuS@CTMAB electrode, EIS measurements were conducted (Figure 2e). Every single Nyquist plot after different cycles consists of one semicircle in the high to medium frequency range and one inclined line in the low-frequency region, which represents the charge-transfer resistance (R_{ct}) and Warburg resistance, respectively. Moreover, the simulation results of the EIS spectra are given in Table S1. The R_{ct} of the CuS@CTMAB electrode slightly increases from the 10th to 50th cycles, possibly due to the self-stabilization of the reaction interface, while the R_{ct} maintains unchanged from the 50th to 100th cycles, implying the establishment of stable electrode/electrolyte interphase. Furthermore, according to the GITT curves (Figure S3), the diffusion coefficient ($D_{Zn^{2+}}$) for Zn^{2+} intercalation into CuS@CTMAB is calculated to be around 10^{-10} to 10^{-12} cm^2 s^{-1} (Figure 2f) by the GITT method (galvanostatic intermittent titration technique), which is even comparable to that of typical intercalation-type Zn^{2+} storage materials including V$_2$O$_5$,[13] Na$_2$V$_6$O$_{16}$·1.63H$_2$O,[50] α-MnO$_2$,[11] ZnMn$_2$O$_4$,[51] and Sn^{4+}−Ti$_2$CT$_x$/C (for the related values, see Table S2),[52] indicating that the material possesses good kinetic characteristics.
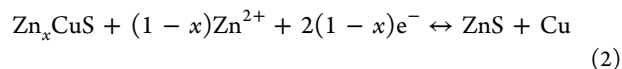
3.3. Mechanism Investigation. To further understand the Zn^{2+} storage mechanism of CuS@CTMAB upon electrochemical charge–discharge processes, various ex situ characterizations such as TEM, XRD, Raman, and XPS were also conducted (Figure 3). After being discharged to 0.3 V in the

initial cycle (Figure 3a), the CuS@CTMAB particle basically preserves its original morphology; no cracking or pulverization was detected, suggesting its excellent structural integrity during the electrochemical reaction process. The locally enlarged HR-TEM images (Figure 3, parts b and c) depict clear lattice fringes with spacing distances of 0.33 and 0.20 nm, implying the existence of ZnS(101) and Cu(111) planes, respectively. Moreover, the uniform distribution of Zn element in the elemental mapping image of the fully discharged CuS@CTMAB electrode also intuitively verifies the insertion of Zn^{2+} (Figure 3d). The crystalline structure evolution was investigated by ex situ XRD analysis of the CuS@CTMAB electrodes using carbon cloth as the current collector at different charge/discharge states (Figure 3e–i). At stage I (A to C), the characteristic peaks of CuS at 47.7° shift to the lower Bragg positions, demonstrating the lattice spacing expansion of CuS induced by Zn^{2+} intercalation (Figure 3f). At stage II (C to D), the characteristic peaks of CuS disappear; instead, a new peak at 47.5° appears corresponding to ZnS (JCPDS no. 89-2158), demonstrating a conversion reaction. Another compelling evidence of the conversion reaction is the emergence of three strong peaks at 43.4°, 50.5°, and 74.2° during the last stage of the Zn^{2+} insertion process (Figure 3, parts g and h), which can be well-indexed to metallic Cu (JCPDS no. 70-3039). For the charging process, these newly generated peaks of Cu further disappear at stage III (D to E), and the characteristic peaks of CuS reoccur upon charging (stage IV, E to G). Moreover, the periodic transformation of CuS and Cu during cycling is also observed in the CuS@CTMAB electrodes after different cycles (Figures S4 and S5a). Ex situ Raman spectra were also obtained to further confirm the electrochemical reaction mechanism (Figure 3j). The pristine CuS@CTMAB shows a broad peak located at ~149.6 cm^{-1}. Upon discharging, the peak intensity of CuS decreases gradually. Meanwhile, another prominent peak appears at ~161.7 cm^{-1} and become stronger progressively at stage II, matching well with the Zn−S vibrations of ZnS.[53] As the peak intensity of CuS recovers again during the charge process, the intensity of the ZnS drops. Such a reversible change can also be verified in CuS@CTMAB electrodes after different cycles (Figure S5b). On the basis of the above analysis, it is evident that the Zn^{2+} storage of CuS@CTMAB is a two-step process combining both intercalation and conversion reactions, which can be summarized as follows:
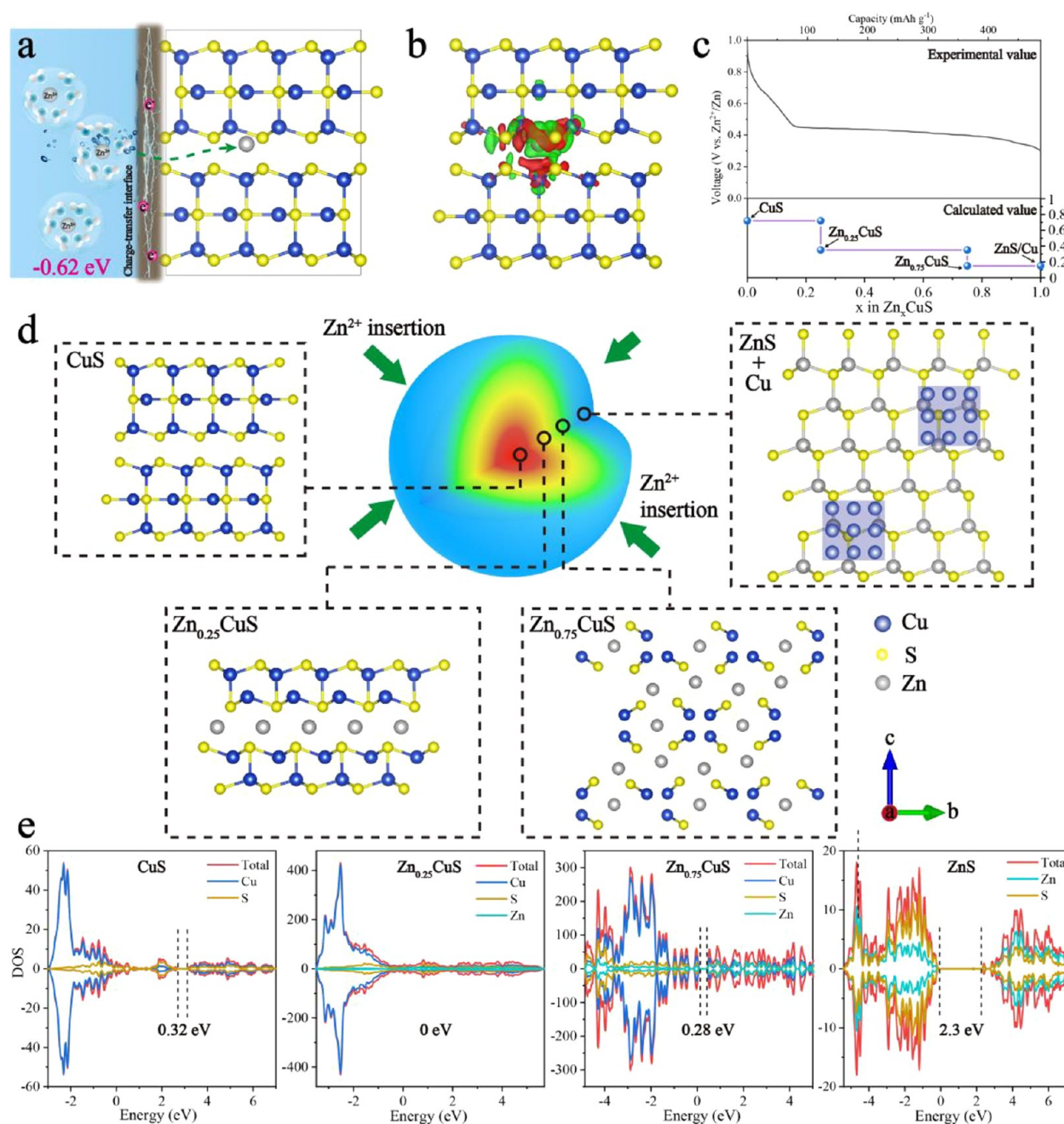
intercalation:

$$CuS + xZn^{2+} + 2xe^- \leftrightarrow Zn_xCuS \qquad (1)$$

conversion:

$$Zn_xCuS + (1-x)Zn^{2+} + 2(1-x)e^- \leftrightarrow ZnS + Cu \qquad (2)$$

In the first step, Zn^{2+} intercalation into the CuS host structure occurs, which results in the lattice expansion. Zn$_x$CuS then converts to ZnS and metallic Cu, contributing to an extra Zn^{2+} storage capacity. Particularly, the reversible phase transformation from ZnS and Cu products to the original CuS phase is also observed during the Zn^{2+} extraction process. We also carried out XPS to probe the chemical nature variation of CuS@CTMAB during cycling. As shown in Figure 3k, no signal for Zn element can be detected in the pristine CuS@CTMAB electrode, whereas two distinct peaks located at 1022.7 and 1045.8 eV are observed in the fully discharged state

Figure 4. (a) Schematic of the initial Zn^{2+} intercalation sites and corresponding intercalation energy in CuS. (b) Charge transfer from CuS to Zn. The red and green regions represent electron accumulation and depletion zones, respectively. (c) The comparison between the initial galvanostatic discharge curve and the theoretical voltage profile obtained from the DFT calculation. (d) Schematic illustrating the reaction pathway of Zn^{2+} in CuS. (e) DOS of CuS, $Zn_{0.25}CuS$, $Zn_{0.75}CuS$, and ZnS.

corresponding to Zn $2p_{3/2}$ and $2p_{1/2}$, indicating the successful accommodation of Zn^{2+}. When charged to 0.9 V, the peak intensity of Zn decreases accordingly, but does not vanish thoroughly, implying that partially inserted Zn^{2+} ions are trapped in CuS@CTMAB. This consequence coincides with the observed nonreversible capacity loss during the initial electrochemical cycle in Figure 2b. Interesting, the peak intensity of Zn after two cycles is close to that after one cycle, suggesting that the irreversible insertion of Zn^{2+} mainly occurs during the initial charge−discharge process. The Auger Cu LMM spectra of the pristine and fully discharged/charged states are shown in Figure 3l. The peak of the pristine CuS@CTMAB electrode is located at 917.8 eV, in agreement with

that of the previously reported CuS. When discharged to 0.3 V, the binding energy shifts to a lower value of 917.0 eV, implying the reduction between Cu^{2+} and Cu^0. Moreover, the peak recovers to 917.7 eV again at the fully charged states, revealing the reversible electrochemical reduction of the Cu^{2+}/Cu^0 couple.

DFT calculation was further employed to get deeper insight into the Zn^{2+} storage mechanism of CuS (Figure 4). As shown in Figure 4a, the most stable Zn^{2+} intercalation sites are located at the interlayer spaces in CuS. The large negative intercalation energy of −0.62 eV implies that the process of Zn^{2+} ions passing through the charge-transfer interface into the lattice host of CuS is favorable from the energy profile. As shown in
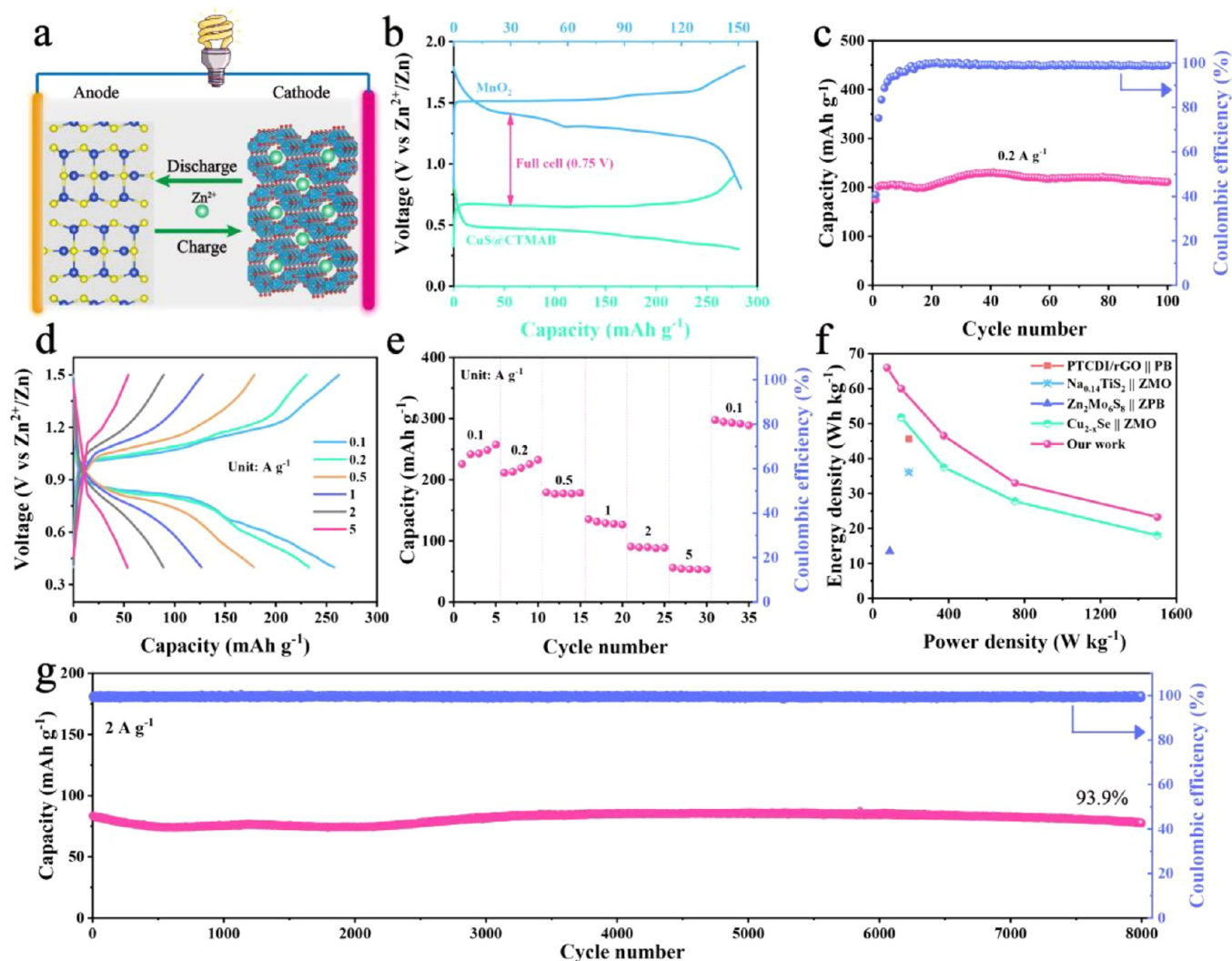
Figure 5. Electrochemical performance of zinc-ion full batteries using CuS@CTMAB as anodes and ZMO as cathodes. (a) Schematic illustration of the working mechanism of the CuS@CTMAB||ZMO zinc-ion full battery. (b) Representative discharge−charge profiles of the MnO$_2$ cathode and CuS@CTMAB anode, respectively. (c) Cycling performance of the CuS@CTMAB||ZMO cell. (d) Typical charge−discharge profiles and (e) rate performance of the CuS@CTMAB||ZMO cell. (f) Ragone plots of the CuS@CTMAB||ZMO cell, compared with previously reported rocking-chair zinc-ion full batteries. (g) Long-term cycling performance of the CuS@CTMAB||ZMO cell at 2 A g^{-1}.

Figure 4b, the intercalation of Zn^{2+} into CuS creates several electron accumulation zones near the neighboring Cu and S atoms, which may act as the local built-in electric field to enhance fast charge transportation. On the basis of the structural evolution of CuS obtained from the ex situ XRD and Raman results, the phase transformation and theoretical voltage profiles of CuS are also investigated using first-principles calculations according to the following relation:

$$V(x) = -\frac{\mu_{Zn}(x) - \mu_{Zn}^0}{2e} \tag{3}$$

where $\mu_{Zn}(x)$ is the Zn chemical potential of Zn$_x$CuS and μ_{Zn}^0 is the Zn chemical potential of metallic Zn.[54] The simulated voltage profiles are basically in agreement with the experimental voltage curves at the current density of 0.2 A g^{-1} (Figure 4c), demonstrating that the calculated reaction pathway of Zn^{2+} in CuS is reasonable. As illustrated in Figure 4d, Zn^{2+} ions are preferentially intercalated into the interlayer active sites of CuS to form an intermediate phase of Zn$_{0.25}$CuS. Afterward, the intercalation of Zn^{2+} ions continues to proceed

in the residual empty sites of CuS until $x = 0.75$. Finally, Zn^{2+} insertion over $x = 0.75$ converts the intercalated structure Zn$_x$CuS into nanosized Cu with high electrochemical activity embedded in a ZnS matrix through the conversion-type mechanism. The evolution described here is consistent with the experimental characterizations. Because the electrochemical process is closely associated with the reaction depth, keeping the unobstructed electronic conduction between different intermediate phases is also necessary for facile charge storage. Density of states (DOS) structures of CuS, Zn$_{0.25}$CuS, Zn$_{0.75}$CuS, and ZnS are shown in Figure 4e. It can be seen that CuS is a good electronic conductor with a small band gap of 0.32 eV. Interestingly, the insertion of Zn^{2+} into CuS to form Zn$_x$CuS will further improve its electron transport properties, and the band gap of Zn$_{0.25}$CuS is even reduced to 0 eV to display metallic conductivity. When the insertion of Zn^{2+} is over $x = 0.75$, one of the conversion products (ZnS) is an n-type semiconductor with a moderate band gap of 2.3 eV. However, the simultaneously generated Cu nanoparticles
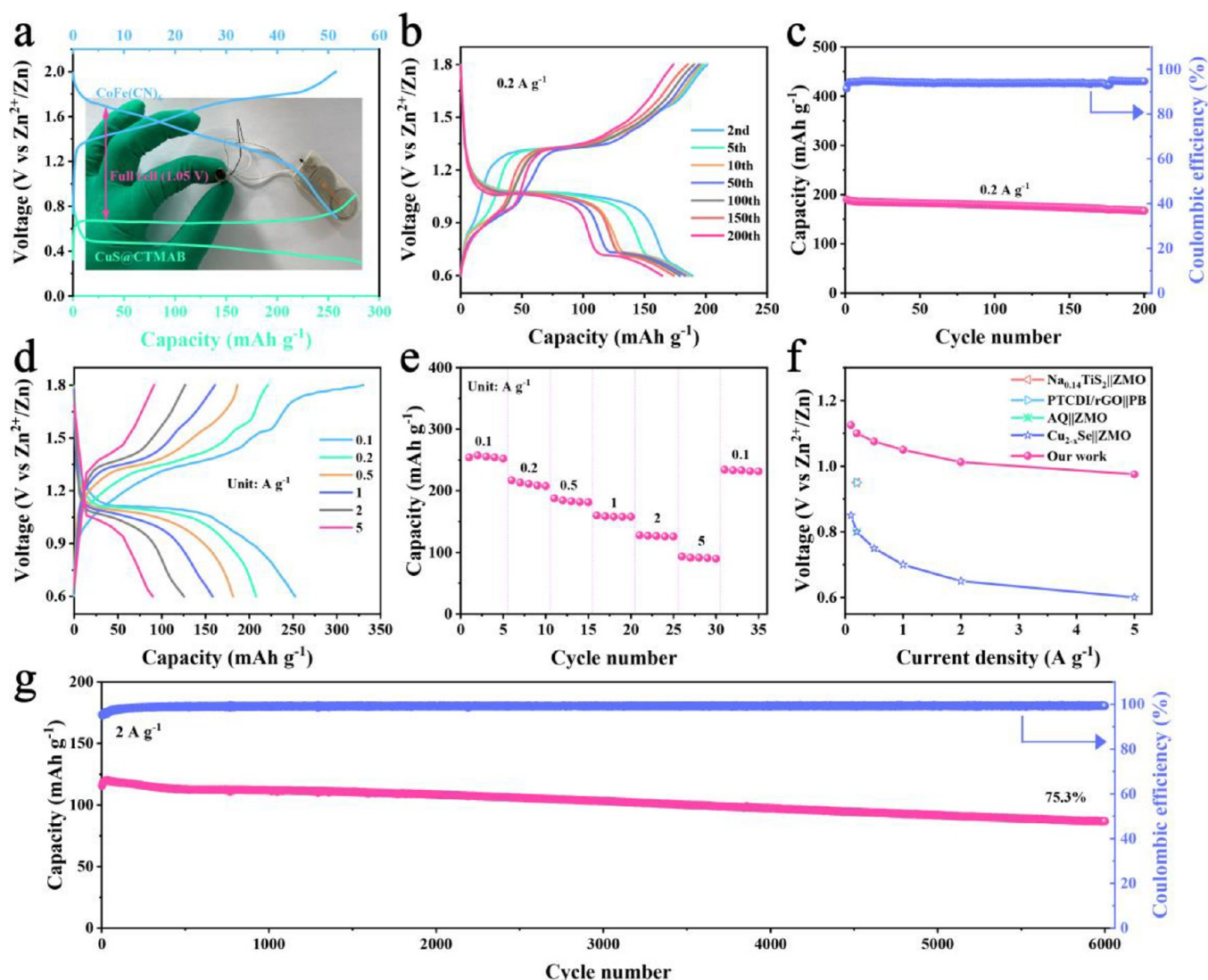
Figure 6. Electrochemical performance of zinc-ion full batteries using CuS@CTMAB as anodes and ZPB as cathodes. (a) Representative charge−discharge profiles of the PB cathode and CuS@CTMAB anode, respectively (inset is the photograph of an electric fan powered by two CuS@CTMAB‖ZPB cells). (b) Typical voltage profiles and (c) cycling performance of the CuS@CTMAB‖ZPB cell. (d) Typical charge−discharge profiles and (e) rate performance of the CuS@CTMAB‖ZPB cell at various current densities. (f) The average operating voltages at various current densities, in comparison with other rocking-chair ZIBs. (g) Long-term cycling performance of the CuS@CTMAB‖ZPB cell at 2 A g^{-1}.

embedded in the ZnS matrix will serve as relay points to ensure fast electron transport.

3.4. Electrochemical Performance of CR-2032-Type Full Cells. The suitable Zn^{2+} insertion potential, high reversible capacity, and good rate capability render the CuS@CTMAB electrode a promising anode for zinc-ion full batteries. According to the capacity matching principle,[55] two kinds of cathodes were adopted to match with the CuS@CTMAB anode to fabricate zinc-ion full batteries, and the electrochemical performance was evaluated systematically. First, the widely used MnO_2 electrode was preintercalated with Zn^{2+} in half-cells and disassembled to be applied as the cathode (denoted as ZMO). In the CuS@CTMAB‖ZMO ZIB prototype (Figure 5a), Zn^{2+} ions can be shuttled from the ZMO cathode acting as the zinc-ion source to the CuS@CTMAB anode receiving the zinc ion during discharging and vice versa reversibly for the charging process. This is referred to as a rocking-chair zinc-ion battery, yielding a typical operating voltage of ∼0.75 V (Figure 5b). The practical

capacity of the CuS@CTMAB‖ZMO full cell with capacity limited by the CuS anode reaches 201.9 mAh g^{-1} at 0.1 A g^{-1} in the voltage range of 0.4−1.5 V (Figure 5c). After 100 cycles, a high reversible capacity of 211.1 mAh g^{-1} was retained at an average CE of 99.3%. As shown in Figure S6, the discharge−charge voltage curves for different cycles almost coincide with each other. Moreover, the peak obtained from the dQ/dV discharge curves remains consistent at around 0.8 V without any detectable voltage decay during cycling (Figure S7), demonstrating the highly reversible electrochemical reactions and small electrochemical polarization in the CuS@CTMAB‖ZMO battery system. The rate performance of the CuS@CTMAB‖ZMO cell is shown in Figure 5, parts d and e. As the current density increases from 0.1 to 0.2, 0.5, 1, 2, and 5 A g^{-1} stepwise, the average discharge capacities slowly decrease from 243.3 to 220.4, 177.7, 130.0, 89.3, and 54.2 mAh g^{-1}. The Ragone plots shown in Figure 5f reveal that the maximum energy density and power density of the CuS@CTMAB‖ZMO cell can reach 66 Wh kg^{-1} and 1500 W kg^{-1} at current

I

densities ranging from 0.1 to 5 A g^{-1}, respectively. Clearly, the CuS@CTMAB∥ZMO cell delivers superior electrochemical performance compared to the state-of-the-art rocking-chair ZIBs, such as PTCDI/rGO∥PB (Prussian blue),[56] Na$_{0.14}$TiS$_2$∥ZMO,[36] Zn$_2$Mo$_6$S$_6$∥ZPB (Zn^{2+}-preintercalated PB),[57] and Cu$_{2-x}$Se∥ZMO.[37] The detailed information is provided in Table S3. To further examine the performance under more demanding conditions, long-term galvanostatic cycling tests at a high current density of 2 A g^{-1} were carried out (Figure 5g). The CuS@CTMAB∥ZMO cell still maintains the specific capacity of 78.5 mAh g^{-1} with an exceptional capacity retention of 93.9% up to 8000 cycles, which corresponds to only 0.00076% capacity decay per cycle. Meanwhile, the CE can keep around 100% without obvious fluctuation during the whole electrochemical cycling process, demonstrating efficient ion and electron transfer and facile Zn^{2+} ion insertion and extraction in the CuS@CTMAB∥ZMO rocking-chair ZIB. In addition, a large-size CuS@CTMAB∥ZMO pouch cell was also fabricated to examine its potential in practical applications (Figures S8 and S9), which can retain a high capacity retention of 94.5% after 50 cycles at 0.2 A g^{-1}.

Although the CuS@CTMAB∥ZMO rocking-chair ZIBs have achieved relatively high energy density and excellent cycling stability, there are still advancement spaces in terms of the working voltage and rate performance. Hence, we also designed another rocking-chair ZIB system by coupling the CuS@CTMAB anode with the CoFe(CN)$_6$ Prussian blue (denoted as ZPB; for the XRD pattern of the precursor see Figure S10) cathode (Figure 6). Benefiting from the inherent high-voltage features of the PB cathode, the CuS@CTMAB∥ZPB cell can output a higher average working voltage of ∼1.05 V (Figure 6a). In addition, two such cells can successfully drive an electric fan (inset in Figure 6a), showing its potential in practical applications. Noteworthily, the discharge voltage curves of the CuS@CTMAB∥ZPB cell at 0.2 A g^{-1} are rather flat (Figure 6b). It is generally accepted that keeping a relatively constant output voltage can effectively improve the utilization efficiency of electric energy in batteries. As shown in Figure 6c, the CuS@CTMAB∥ZPB cell exhibits an initial discharge capacity of 190.5 mAh g^{-1} at the current density of 0.2 A g^{-1}. After 200 cycles, it also delivers a reversible capacity of 167.4 mAh g^{-1}, implying good cycling stability. Due to the improved ion transport in the PB cathode compared to the MnO$_2$ cathode, the high rate performance of the CuS@CTMAB anode is no longer critically restricted, leading to the enhanced rate performance of the CuS@CTMAB∥ZPB cell (Figure 6, parts d and e). It can deliver discharge capacities of 255.7 to 211.4, 182.9, 160.0, and 126.5 mAh g^{-1} at 0.1, 0.2, 0.5, 1, and 2 A g^{-1}, respectively. The outstanding rate performance reveals that the maximum energy density and power density of the CuS@CTMAB∥ZPB cell can reach 42 Wh kg^{-1} and 2100 W kg^{-1} at the current densities ranging from 0.1 to 2 A g^{-1}, respectively (Figure S12). Even at 5 A g^{-1}, which corresponds to a 66 s ultrafast discharge process, a considerable capacity of 91.4 mAh g^{-1} is achieved. The battery operating voltage is also a significant indicator for practical applications. As shown in Figure 6f, the average operating voltage of the CuS@CTMAB∥ZPB cell is higher than other previously reported rocking-chair ZIBs. Furthermore, the voltage drop of the CuS@CTMAB∥ZPB cell is principally negligible as the current density increases, revealing a small polarization influence. Subsequently, the long-term cycling stability of the CuS@CTMAB∥ZPB cell was also investigated (Figure 6g). The CuS@

CTMAB∥ZPB cell exhibits a high reversible capacity of 86.8 mAh g^{-1} over 6000 cycles at the current density of 2 A g^{-1}, with a meager capacity decay observed. This fading may be mainly due to the intrinsic crystalline structure evolution of PB during repeated cycling.

4. CONCLUSIONS

In conclusion, CTMAB-preintercalated CuS (CuS@CTMAB) was prepared and investigated as a high-capacity anode for rocking-chair ZIBs. CTMAB molecules act as robust pillars to enlarge the interlayer spacing of CuS and thus facilitate the intercalation of Zn^{2+} ions. DFT calculation and ex situ XRD, Raman, XPS, and TEM characterizations demonstrate that CuS@CTMAB experiences a characteristic stepwise intercalation−conversion reaction route during the discharge process (CuS → Zn$_{0.25}$CuS → Zn$_{0.75}$CuS → Cu + ZnS). The coefficient combination of the intercalation and conversion reaction mechanism can not only realize a large Zn^{2+} storage capacity but also contribute to the moderate structure transformation and good electronic conduction during cycling, leading to excellent cycling stability and high rate performance. Most importantly, the CuS@CTMAB anodes were successfully paired with conventional MnO$_2$ and CoFe(CN)$_6$ Prussian blue cathodes to establish rocking-chair zinc-ion full battery systems. Encouragingly, the CuS@CTMAB∥ZMO cell delivers a considerable reversible capacity of 78.5 mAh g^{-1} with an exceptional capacity retention of 93.9% up to 8000 cycles at 2 A g^{-1}. In addition, the CuS@CTMAB∥ZPB cell can output a high average working voltage of ∼1.05 V, which is predominant compared with other reported rocking-chair zinc-ion full batteries. Such innovative rocking-chair ZIB systems based on the high-performance CuS@CTMAB anode hold great potential for large-scale applications.

■ ASSOCIATED CONTENT

ⓢ Supporting Information

The Supporting Information is available free of charge at https://pubs.acs.org/doi/10.1021/acsami.1c21168.

> SEM images of pristine CuS, XRD patterns of the KCoFe(CN)$_6$ sample, ex situ XRD patterns and Raman spectra of CuS@CTMAB electrodes, EIS spectra of CuS@CTMAB electrodes, and electrochemical performance of the CuS@CTMAB electrodes and CuS@CTMAB ∥ZMO and CuS@CTMAB∥ZPB cells (PDF)

■ AUTHOR INFORMATION

Corresponding Authors

Yang Yang − College of Chemistry and Chemical Engineering, Xiamen University, Xiamen 361005, People's Republic of China; Email: yangyang419@xmu.edu.cn

Cheng Chao Li − School of Chemical Engineering and Light Industry, Guangdong University of Technology, Guangzhou 510006, People's Republic of China; ◉ orcid.org/0000-0003-2434-760X; Email: licc@gdut.edu.cn

Authors

Zeheng Lv − School of Chemical Engineering and Light Industry, Guangdong University of Technology, Guangzhou 510006, People's Republic of China

Bo Wang − School of Chemical Engineering and Light Industry, Guangdong University of Technology, Guangzhou 510006, People's Republic of China

Minghui Ye − *School of Chemical Engineering and Light Industry, Guangdong University of Technology, Guangzhou 510006, People's Republic of China*

Yufei Zhang − *School of Chemical Engineering and Light Industry, Guangdong University of Technology, Guangzhou 510006, People's Republic of China*

■ ACKNOWLEDGMENTS

■ REFERENCES

(1) Tarascon, J. M.; Armand, M. Issues and Challenges Facing Rechargeable Lithium Batteries. *Nature* **2001**, *414*, 359−367.

(2) Wang, M.; Zheng, X.; Zhang, X.; Chao, D.; Qiao, S. Z.; Alshareef, H. N.; Cui, Y.; Chen, W. Opportunities of Aqueous Manganese-Based Batteries with Deposition and Stripping Chemistry. *Adv. Energy Mater.* **2021**, *11*, 2002904.

(3) Konarov, A.; Voronina, N.; Jo, J. H.; Bakenov, Z.; Sun, Y.-K.; Myung, S.-T. Present and Future Perspective on Electrode Materials for Rechargeable Zinc-Ion Batteries. *ACS Energy Lett.* **2018**, *3*, 2620−2640.

(4) Chen, Z.; Belharouak, I.; Sun, Y.-K.; Amine, K. Titanium-Based Anode Materials for Safe Lithium-Ion Batteries. *Adv. Funct. Mater.* **2013**, *23*, 959−969.

(5) Liu, Y. Y.; He, G. J.; Jiang, H.; Parkin, I. P.; Shearing, P. R.; Brett, D. J. L. Cathode Design for Aqueous Rechargeable Multivalent Ion Batteries: Challenges and Opportunities. *Adv. Funct. Mater.* **2021**, *31*, 2010445.

(6) Liang, T. T.; Hou, R. L.; Dou, Q. Y.; Zhang, H. Z.; Yan, X. B. The Applications of Water-in-Salt Electrolytes in Electrochemical Energy Storage Devices. *Adv. Funct. Mater.* **2021**, *31*, 2006749.

(7) Demir-Cakan, R.; Palacin, M. R.; Croguennec, L. Rechargeable Aqueous Electrolyte Batteries: From Univalent to Multivalent Cation Chemistry. *J. Mater. Chem. A* **2019**, *7*, 20519−20539.

(8) Hao, J. N.; Li, X. L.; Zeng, X. H.; Li, D.; Mao, J. F.; Guo, Z. P. Deeply Understanding the Zn Anode Behaviour and Corresponding Improvement Strategies in Different Aqueous Zn-Based Batteries. *Energy Environ. Sci.* **2020**, *13*, 3917−3949.

(9) Yong, B.; Ma, D.; Wang, Y.; Mi, H.; He, C.; Zhang, P. Understanding the Design Principles of Advanced Aqueous Zinc-Ion Battery Cathodes: From Transport Kinetics to Structural Engineering, and Future Perspectives. *Adv. Energy Mater.* **2020**, *10*, 2002354.

(10) Huang, J.; Zhou, J.; Liang, S. Guest Pre-Intercalation Strategy to Boost the Electrochemical Performance of Aqueous Zinc-Ion Battery Cathodes. *Acta Phys. -Chim. Sin.* **2020**, *37*, 2005020.

(11) Wu, B.; Zhang, G.; Yan, M.; Xiong, T.; He, P.; He, L.; Xu, X.; Mai, L. Graphene Scroll-Coated Alpha-MnO2 Nanowires as High-Performance Cathode Materials for Aqueous Zn-Ion Battery. *Small* **2018**, *14*, 1703850.

(12) Chao, D. L.; Zhou, W. H.; Ye, C.; Zhang, Q. H.; Chen, Y. G.; Gu, L.; Davey, K.; Qiao, S. Z. An Electrolytic Zn-MnO2 Battery for High-Voltage and Scalable Energy Storage. *Angew. Chem., Int. Ed.* **2019**, *58*, 7823−7828.

(13) Zhang, N.; Dong, Y.; Jia, M.; Bian, X.; Wang, Y.; Qiu, M.; Xu, J.; Liu, Y.; Jiao, L.; Cheng, F. Rechargeable Aqueous Zn−V2O5 Battery with High Energy Density and Long Cycle Life. *ACS Energy Lett.* **2018**, *3*, 1366−1372.

(14) Yang, X.; Deng, W.; Chen, M.; Wang, Y.; Sun, C.-F. Mass-Producible, Quasi-Zero-Strain, Lattice-Water-Rich Inorganic Open-Frameworks for Ultrafast-Charging and Long-Cycling Zinc-Ion Batteries. *Adv. Mater.* **2020**, *32*, 2003592.

(15) Li, W.; Wang, K. L.; Cheng, S. J.; Jiang, K. A Long-Life Aqueous Zn-Ion Battery Based on Na3V2(PO4)2F3 Cathode. *Energy Storage Mater.* **2018**, *15*, 14−21.

(16) Liu, Z.; Pulletikurthi, G.; Endres, F. A Prussian Blue/Zinc Secondary Battery with a Bio-Ionic Liquid-Water Mixture as Electrolyte. *ACS Appl. Mater. Interfaces* **2016**, *8*, 12158−64.

(17) Tie, Z.; Niu, Z. Design Strategies for High-Performance Aqueous Zn/Organic Batteries. *Angew. Chem., Int. Ed.* **2020**, *59*, 21293−21303.

(18) Wang, F.; Borodin, O.; Gao, T.; Fan, X.; Sun, W.; Han, F.; Faraone, A.; Dura, J. A.; Xu, K.; Wang, C. Highly Reversible Zinc Metal Anode for Aqueous Batteries. *Nat. Mater.* **2018**, *17*, 543−549.

(19) Zheng, J.; Zhao, Q.; Tang, T.; Yin, J.; Quilty, C. D.; Renderos, G. D.; Liu, X.; Deng, Y.; Wang, L.; Bock, D. C.; Jaye, C.; Zhang, D.; Takeuchi, E. S.; Takeuchi, K. J.; Marschilok, A. C.; Archer, L. A. Reversible Epitaxial Electrodeposition of Metals in Battery Anodes. *Science* **2019**, *366*, 645−648.

(20) Blanc, L. E.; Kundu, D.; Nazar, L. F. Scientific Challenges for the Implementation of Zn-Ion Batteries. *Joule* **2020**, *4*, 771−799.

(21) Wang, T.; Li, C.; Xie, X.; Lu, B.; He, Z.; Liang, S.; Zhou, J. Anode Materials for Aqueous Zinc Ion Batteries: Mechanisms, Properties, and Perspectives. *ACS Nano* **2020**, *14*, 16321−16347.

(22) Zhang, N.; Huang, S.; Yuan, Z.; Zhu, J.; Zhao, Z.; Niu, Z. Direct Self-Assembly of MXene on Zn Anodes for Dendrite-Free Aqueous Zinc-Ion Batteries. *Angew. Chem., Int. Ed.* **2021**, *60*, 2861−2865.

(23) Hao, J.; Li, B.; Li, X.; Zeng, X.; Zhang, S.; Yang, F.; Liu, S.; Li, D.; Wu, C.; Guo, Z. An In-Depth Study of Zn Metal Surface Chemistry for Advanced Aqueous Zn-Ion Batteries. *Adv. Mater.* **2020**, *32*, 2003021.

(24) Liu, M.; Cai, J.; Ao, H.; Hou, Z.; Zhu, Y.; Qian, Y. NaTi2(PO4)3 Solid-State Electrolyte Protection Layer on Zn Metal Anode for Superior Long-Life Aqueous Zinc-Ion Batteries. *Adv. Funct. Mater.* **2020**, *30*, 2004885.

(25) Zhao, Z. M.; Zhao, J. W.; Hu, Z. L.; Li, J. D.; Li, J. J.; Zhang, Y. J.; Wang, C.; Cui, G. L. Long-Life and Deeply Rechargeable Aqueous Zn Anodes Enabled by a Multifunctional Brightener-Inspired Interphase. *Energy Environ. Sci.* **2019**, *12*, 1938−1949.

(26) Yan, H.; Li, S.; Nan, Y.; Yang, S.; Li, B. Ultrafast Zinc−Ion−Conductor Interface toward High-Rate and Stable Zinc Metal Batteries. *Adv. Energy Mater.* **2021**, *11*, 2100186.

(27) Liu, B. T.; Wang, S. J.; Wang, Z. L.; Lei, H.; Chen, Z. T.; Mai, W. J. Novel 3D Nanoporous Zn-Cu Alloy as Long-Life Anode toward High-Voltage Double Electrolyte Aqueous Zinc-Ion Batteries. *Small* **2020**, *16*, 2001323.

(28) Tian, H.; Li, Z.; Feng, G.; Yang, Z.; Fox, D.; Wang, M.; Zhou, H.; Zhai, L.; Kushima, A.; Du, Y.; et al. Stable, High-Performance, Dendrite-Free, Seawater-Based Aqueous Batteries. *Nat. Commun.* **2021**, *12*, 237.

(29) Ma, L.; Li, Q.; Ying, Y.; Ma, F.; Chen, S.; Li, Y.; Huang, H.; Zhi, C. Toward Practical High-Areal-Capacity Aqueous Zinc-Metal Batteries: Quantifying Hydrogen Evolution and a Solid-Ion Conductor for Stable Zinc Anodes. *Adv. Mater.* **2021**, *33*, 2007406.

(30) Zeng, X.; Mao, J.; Hao, J.; Liu, J.; Liu, S.; Wang, Z.; Wang, Y.; Zhang, S.; Zheng, T.; Liu, J.; Rao, P.; Guo, Z. Electrolyte Design for In Situ Construction of Highly Zn (2+) -Conductive Solid Electrolyte Interphase to Enable High-Performance Aqueous Zn-Ion Batteries under Practical Conditions. *Adv. Mater.* **2021**, *33*, 2007416.

(31) Winter, M.; Barnett, B.; Xu, K. Before Li Ion Batteries. *Chem. Rev.* **2018**, *118*, 11433−11456.

(32) Yoshino, A. The Birth of the Lithium-Ion Battery. *Angew. Chem., Int. Ed.* **2012**, *51*, 5798−800.

(33) Tian, Y.; An, Y.; Wei, C.; Xi, B.; Xiong, S.; Feng, J.; Qian, Y. Recent Advances and Perspectives of Zn-Metal Free "Rocking-Chair"-Type Zn-Ion Batteries. *Adv. Energy Mater.* **2021**, *11*, 2002529.

(34) Xiong, T.; Zhang, Y. X.; Wang, Y. M.; Lee, W. S. V.; Xue, J. M. Hexagonal MoO3 as a Zinc Intercalation Anode towards Zinc Metal-Free Zinc-Ion Batteries. *J. Mater. Chem. A* **2020**, *8*, 9006−9012.

(35) Cheng, Y.; Luo, L.; Zhong, L.; Chen, J.; Li, B.; Wang, W.; Mao, S. X.; Wang, C.; Sprenkle, V. L.; Li, G.; Liu, J. Highly Reversible Zinc-Ion Intercalation into Chevrel Phase Mo6S8 Nanocubes and Applications for Advanced Zinc-Ion Batteries. *ACS Appl. Mater. Interfaces* **2016**, *8*, 13673−7.

(36) Li, W.; Wang, K.; Cheng, S.; Jiang, K. An Ultrastable Presodiated Titanium Disulfide Anode for Aqueous "Rocking-Chair" Zinc Ion Battery. *Adv. Energy Mater.* **2019**, *9*, 1900993.

(37) Yang, Y.; Xiao, J.; Cai, J.; Wang, G.; Du, W.; Zhang, Y.; Lu, X.; Li, C. C. Mixed-Valence Copper Selenide as an Anode for Ultralong Lifespan Rocking-Chair Zn-Ion Batteries: An Insight into its Intercalation/Extraction Kinetics and Charge Storage Mechanism. *Adv. Funct. Mater.* **2021**, *31*, 2005092.

(38) Whittingham, M. S. Ultimate Limits to Intercalation Reactions for Lithium Batteries. *Chem. Rev.* **2014**, *114*, 11414−43.

(39) Reddy, M. V.; Subba Rao, G. V.; Chowdari, B. V. R. Metal Oxides and Oxysalts as Anode Materials for Li Ion Batteries. *Chem. Rev.* **2013**, *113*, 5364−5457.

(40) Li, H.; Wang, Y. H.; Huang, J. X.; Zhang, Y. Y.; Zhao, J. B. Microwave-Assisted Synthesis of CuS/Graphene Composite for Enhanced Lithium Storage Properties. *Electrochim. Acta* **2017**, *225*, 443−451.

(41) Xie, F.; Li, H.; Wang, X.; Zhi, X.; Chao, D.; Davey, K.; Qiao, S. Z. Mechanism for Zincophilic Sites on Zinc-Metal Anode Hosts in Aqueous Batteries. *Adv. Energy Mater.* **2021**, *11*, 2003419.

(42) Hao, J.; Yuan, L.; Johannessen, B.; Zhu, Y.; Jiao, Y.; Ye, C.; Xie, F.; Qiao, S. Z. Studying the Conversion Mechanism to Broaden Cathode Options in Aqueous Zinc-Ion Batteries. *Angew. Chem., Int. Ed.* **2021**, *60*, 25114−25121.

(43) Xiao, Y. H.; Su, D. C.; Wang, X. Z.; Wu, S. D.; Zhou, L. M.; Shi, Y.; Fang, S. M.; Cheng, H. M.; Li, F. CuS Microspheres with Tunable Interlayer Space and Micropore as a High-Rate and Long-Life Anode for Sodium-Ion Batteries. *Adv. Energy Mater.* **2018**, *8*, 1800930.

(44) Ma, L. T.; Chen, S. M.; Long, C. B.; Li, X. L.; Zhao, Y. W.; Liu, Z. X.; Huang, Z. D.; Dong, B. B.; Zapien, J. A.; Zhi, C. Y. Achieving High-Voltage and High-Capacity Aqueous Rechargeable Zinc Ion Battery by Incorporating Two-Species Redox Reaction. *Adv. Energy Mater.* **2019**, *9*, 1902446.

(45) Perdew, J. P.; Burke, K.; Ernzerhof, M. Generalized Gradient Approximation Made Simple. *Phys. Rev. Lett.* **1996**, *77*, 3865−3868.

(46) Kresse, G.; Joubert, D. From Ultrasoft Pseudopotentials to the Projector Augmented-Wave Method. *Phys. Rev. B* **1999**, *59*, 1758−1775.

(47) Dong, W.; Shi, J.-L.; Wang, T.-S.; Yin, Y.-X.; Wang, C.-R.; Guo, Y.-G. 3D Zinc@Carbon Fiber Composite Framework Anode for Aqueous Zn−MnO2 Batteries. *RSC Adv.* **2018**, *8*, 19157−19163.

(48) Tang, B.; Shan, L.; Liang, S.; Zhou, J. Issues and Opportunities Facing Aqueous Zinc-Ion Batteries. *Energy Environ. Sci.* **2019**, *12*, 3288−3304.

(49) Ding, J.; Gao, H.; Ji, D.; Zhao, K.; Wang, S.; Cheng, F. Vanadium-Based Cathodes for Aqueous Zinc-Ion Batteries: From Crystal Structures, Diffusion Channels to Storage Mechanisms. *J. Mater. Chem. A* **2021**, *9*, 5258−5275.

(50) Hu, P.; Zhu, T.; Wang, X.; Wei, X.; Yan, M.; Li, J.; Luo, W.; Yang, W.; Zhang, W.; Zhou, L.; Zhou, Z.; Mai, L. Highly Durable Na2V6O16.1.63H2O Nanowire Cathode for Aqueous Zinc-Ion Battery. *Nano Lett.* **2018**, *18*, 1758−1763.

(51) Zhang, N.; Cheng, F.; Liu, Y.; Zhao, Q.; Lei, K.; Chen, C.; Liu, X.; Chen, J. Cation-Deficient Spinel ZnMn2O4 Cathode in Zn(CF3SO3)2 Electrolyte for Rechargeable Aqueous Zn-Ion Battery. *J. Am. Chem. Soc.* **2016**, *138*, 12894−12901.

(52) Li, X.; Li, M.; Yang, Q.; Wang, D.; Ma, L.; Liang, G.; Huang, Z.; Dong, B.; Huang, Q.; Zhi, C. Vertically Aligned Sn4+ Preintercalated Ti2CTX MXene Sphere with Enhanced Zn Ion Transportation and Superior Cycle Lifespan. *Adv. Energy Mater.* **2020**, *10*, 2001394.

(53) Kumari, A.; Thakur, N.; Vashishtt, J.; Singh, R. R. Structural, Luminescent and Antimicrobial Properties of ZnS and CdSe/ZnS Quantum Dot Structures Originated by Precursors. *Spectrochim. Acta. A Mol. Biomol. Spectrosc.* **2020**, *229*, 117962.

(54) Park, J. Y.; Kim, S. J.; Chang, J. H.; Seo, H. K.; Lee, J. Y.; Yuk, J. M. Atomic Visualization of a Non-Equilibrium Sodiation Pathway in Copper Sulfide. *Nat. Commun.* **2018**, *9*, 922.

(55) Yuan, L.; Hao, J.; Kao, C.-C.; Wu, C.; Liu, H.-K.; Dou, S.-X.; Qiao, S.-Z. Regulation Methods for the Zn/Electrolyte Interphase and the Effectiveness Evaluation in Aqueous Zn-Ion Batteries. *Energy Environ. Sci.* **2021**, *14*, 5669−5689.

(56) Liu, N.; Wu, X.; Zhang, Y.; Yin, Y.; Sun, C.; Mao, Y.; Fan, L.; Zhang, N. Building High Rate Capability and Ultrastable Dendrite-Free Organic Anode for Rechargeable Aqueous Zinc Batteries. *Adv. Sci.* **2020**, *7*, 2000146.

(57) Chae, M. S.; Hong, S.-T. Prototype System of Rocking-Chair Zn-Ion Battery Adopting Zinc Chevrel Phase Anode and Rhombohedral Zinc Hexacyanoferrate Cathode. *Batteries* **2019**, *5*, 3.